Indian Journal of Pure & Applied Physics
Vol. 62, June 2024, pp. 464-477
DOI: 10.56042/ijpap.v62i6.7996

Realization of All-Optical Full Adder and Subtractor Circuit based on Cross-Phase Modulation in a Phase-Shifted Fiber Bragg Grating

Raj Ranjan Singh[a], Ajay Kumar[a*], Shiva Nand Singh[b] & Ajay Yadav[a]

[a]Fiber optics Laboratory, Department of Electronics and Communication Engineering, National Institute of Technology Jamshedpur, Jharkhand 831 014, India

[b]Department of Electronics and Communication Engineering, National Institute of Technology Jamshedpur, Jharkhand 831 014, India

Received 11 January 2024; accepted 13 February 2024

This study presents a technique for implementing all-optical Full Adder (FA) and Full Subtractor (FS) functionalities utilizing a Fiber Bragg Grating (FBG) structure. The proposed method exploits the cross-phase modulation (XPM) mechanism within a phase-shifted FBG (PSFBG) configuration. An analysis of basic gate operations and corresponding switching phenomena is provided, along with the optimization and implementation of FA and FS circuits using the PSFBG structure. Extensive simulations, validated against conventional circuits and truth tables, demonstrate the efficacy of the proposed approach. The coupled-mode theory governing FBG behavior as an optical switching element is elucidated, along with mathematical descriptions of FBG and PSFBG functionalities for switching applications. MATLAB simulations are employed for comprehensive analysis and validation of the proposed all-optical FA and FS schemes. This work contributes to the advancement of all-optical computing techniques, facilitating efficient high-speed data processing with notable optical communication benefits.

Keywords: Fiber Bragg Grating; Cross-phase modulation; phase-shifted FBG; Full adder and subtractor

1 Introduction

All-optical logic operations, bypassing optical-electrical-optical conversion, are critical for reducing power consumption in the next generation of optical networks and devices. Integrated optical devices, such as couplers and switches, play a vital role in optical data processing and ultra-high-speed optical communication applications. Silberberg *et al.*[1] demonstrated a Ti:LiNbO3-based digital electro-optic switch, achieving wavelength and polarization independence. This four-port integrated optical switch exhibits a step-like response to the applied voltage, enabled by adiabatic eigenmode transformation in an asymmetric waveguide junction. Previous comprehensive reviews have covered various optical switching-related technologies and methods[2]. Recent advancements in ultrafast all-optical switching have contributed to progress in nanophotonics, integrated optics, nonlinear optics, material science, and optical communications[3]. Sasikala *et al.*[4] highlighted the steady advancement of optical switching technology, emphasizing various technologies used in all-optical gates and other switching circuits for all-optical processing. Nozaki *et al.*[5] demonstrated low-energy switching within a few tens of picoseconds using strong carrier-induced nonlinearity in InGaAsP and an ultrasmall photonic crystal nanocavity. Volz, Thomas, *et al.*[6] presented single-photon-based ultrafast all-optical switching. However, waveguide all-optical switching devices may face limitations due to two-photon absorption[7].

Researchers have employed various switching methods to construct optical logic circuits. Mach-Zehnder interferometers (MZIs) enable optical switching based on the electro-optic effect theory, where the change in the refractive index is proportional to the intensity of the applied electric field. The electro-optic effect-based MZI structure facilitates the creation of a variety of logic gates, both combinational and sequential. Numerous studies have reported and reviewed optical switching based on the MZI[8–10]. Kumar *et al.*[11–14] reported MZI-based XOR/XNOR, AND logic gates, and universal logic gates. Kaur *et al.*[15] presented a half adder and half subtractor using the electro-optic effect-based MZI. Amrindra *et al.*[16] reported a 2-4 line and 3-8 line decoder exploiting the electro-optic effect within an MZI made of lithium niobate. Martin *et al.*[17] presented a fast optical flip-flop constructed from two coupled MZIs. Kumar *et al.*[18-19] demonstrated the design of the

---

*Corresponding author: (E-mail: ajay.ece@nitjsr.ac.in)

D flip-flop, T flip-flop, and universal shift register based on the electro-optic effect in an MZI. Additionally, using the MZI structure, Raghuwanshi *et al*.[20] reported optically clocked D flip-flops and showed that the outputs of an optically clocked D flip-flop are provided through an appropriate feedback system with the delay unit. The development of all-optical logic gates heavily depends on SOA, with MZIs serving as the main switching elements. Short switchable SOAs are employed to either compensate for loss or decrease crosstalk[21-22]. Kim *et al*.[23] employed two parallel SOA-MZI devices to design all-optical multiple logic gates, allowing for the simultaneous operation of XOR, NOR, OR, and NAND logic. All-optical decoders and data comparators are implemented at higher data rates by using an optical tree architecture (OTA) in the SOA-based MZI switch[24-26]. The design of a high-speed all-optical ripple carry adder using SOA-MZI. Many researchers have reported temperature, curvature sensors, and refractive index sensors based on the MZI[27-28]. Micro-ring resonators (MRR) with all-optical switching capability attract researchers for ultra-fast optical logic devices and sensors. Rakshit *et al*.[29] analyzed a nonlinear MRR as a switch and used a cascaded MRR for all-optical logical operations. MRRs implement various logic circuits like NAND gates, half adders[30], phase-based logic gates[31], adder/subtractor[32-33], XOR/XNOR, AND full adder/subtractor[34], electro-optic directed optical decoders[35], JK, SR, and T flip-flops[36], D and T flip-flops[37], ripple down counters[38], and optical sequence detectors[39]. MRRs are used for concentration and temperature sensors[40]. A photonic crystal-based MRR detects refractive index[41]. Yadav *et al*.[42] offer an innovative study on designing and analyzing all-optical half- and full-adder/subtractor circuits based on nonlinear asymmetric directional couplers.

The paper presents the design of a full adder and full subtractor incorporating different phase shifts in FBG. The chosen material is a highly nonlinear erbium-doped fiber, contributing to reduced threshold power for switching. Section 2 briefly outlines the coupled-mode theory for the FBG structure, which serves as an optical switching device. Section 3 delves into the mathematical aspects of the FBG structure's switching functionality. In Section 4, the switching mechanism of PSFBG is discussed. The proposed scheme for all-optical full adder and full subtractor, validated through MATLAB simulations, is detailed in Sections 5 and 6, respectively. The paper concludes with a summary of the findings.

2 Coupled Mode Theory for the Fiber Bragg Grating

FBGs are fabricated using various techniques, including the induction of periodic modulation along the refractive index of single-mode optical fibers in the longitudinal direction. These devices represent one of several technologies employed in optical communication systems to enhance their performance. Fig. 1 illustrates the design of a uniform FBG characterized by a consistent modulation of the refractive index. A Bragg grating is formed when a section of germanium-doped single-mode optical fiber undergoes a periodic variation in the refractive index of the core due to exposure to an intense UV light pattern in the 244-248nm bandwidth. Typically, a Bragg grating has a length ranging between 1-20 nm. The reflected light beam exhibits a destructive interference pattern, as each light beam is not in

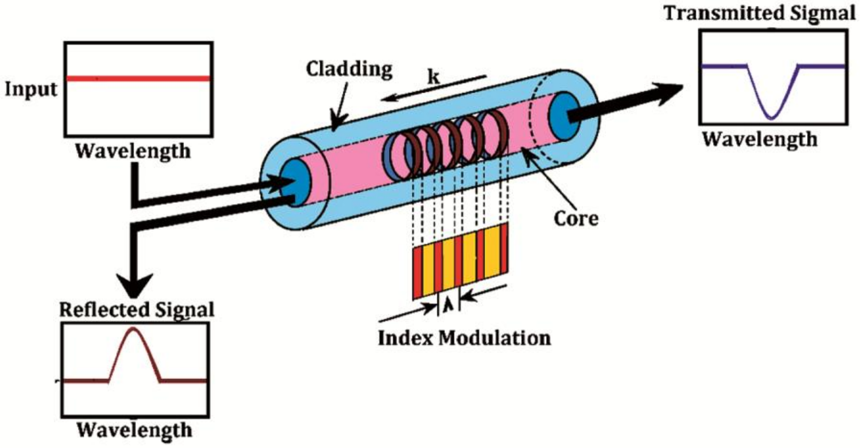

Fig. 1 — Design of uniform FBG exhibiting constant index modulation

phase. According to Bragg's law, the following conditions can be observed:

$$\lambda_B = 2n_0\Lambda \quad \text{... (1)}$$

Where, n_0 is the mean core refractive index and Λ is the grating period of the refractive index perturbation.

The fibre core of FBG, there exists a grating structure as shown in Fig. 2. These are the regular changes in the refractive index that occur inside the core of optical fiber[43].

The refractive index variation can be shown in Eq. 2.

$$n(x,z) = n_1(x) + \delta n(z) \quad \text{... (2)}$$

Now, the value of $\delta n(z)$ can be represented as $\delta n(z) = \Delta n \sin(Kz)$, where $K = \frac{2\pi}{\Lambda}$. Λ is the grating period and K is the grating wave vector. Eq. (2) can be changed and represented as,

$$n^2(x,z) \approx n_1^2(x) + \sigma \sin(Kz), \text{where } \sigma = 2n_1\Delta n$$

$$n^2 = n_1^2 + \sigma \sin\left(\frac{2\pi}{\Lambda}z\right) \quad \text{... (3)}$$

Figure 3 shows two waves propagating in opposite directions, one moving forward and the other moving backward. These two waves together are referred to as the total field. Some amplitude is associated with the forward-moving wave, which is the function of z, represented as A(z), and some with the backward propagating wave, which is denoted as B(z). Using the coupled mode theory, we can find out the evolution of the equation dA/dz and dB/dz. In order to perform the analysis of the slab waveguide with the core refractive index n_1 is required. The wave equation in the slab waveguide can be represented as follows[44].

$$R = \frac{\kappa^2 \sin^2(\gamma L)}{\gamma^2 \cos^2(\gamma L) + \frac{\Gamma^2}{4}\sin^2(\gamma L)} \quad \text{... (4)}$$

Where coupling co-efficient κ is one of the most important parameter, and is shown below;

$$\kappa = \frac{n_1 \Delta n \pi}{2n_{\text{eff}}^2 \Lambda} \text{ for the Bragg Wavelength} \quad \text{... (5)}$$

$\Gamma = K - 2\beta_1$ where β_1 is the propagation constant of the guided wave and L is the grating length.

$$\gamma^2 = \frac{\Gamma^2}{4} - \kappa^2$$

Finally,

$$R = \frac{\kappa^2 \sin^2(\gamma L)}{\left[\frac{\Gamma^2}{4} - \gamma^2 \cos^2(\gamma L)\right]} \quad \text{... (6)}$$

Summary :

$$\left.\begin{aligned} R &= \frac{\kappa^2 \sinh^2(\alpha L)}{\left[\alpha^2 \cosh^2(\alpha L) + \frac{\Gamma^2}{4}\sinh^2(\alpha L)\right]}, \text{where } \left|\frac{1}{\lambda_0} - \frac{1}{\lambda_B}\right| < \frac{\kappa}{2\pi n_{\text{eff}}} \\ R &= \frac{\kappa^2 \sin^2(\gamma L)}{\left[\frac{\Gamma^2}{4} - \gamma^2 \cos^2(\gamma L)\right]}, \left|\frac{1}{\lambda_0} - \frac{1}{\lambda_B}\right| > \frac{\kappa}{2\pi n_{\text{eff}}} \\ R &= \tanh^2(\kappa L), \text{where } \lambda_0 = \lambda_B \end{aligned}\right\} \quad \text{... (7)}$$

Figure 4 shows the reflectivity curve of the fiber Bragg grating structure. Using Eq. (7), the reflectivity curve is obtained for grating length $L = 4\text{mm}$, $n_1 = 1.5, \Delta n = 1.4 \times 10^{-3}$, grating period 535.90nm. Whereas the effective index is $n_{\text{eff}} = 1.447$. Fig. 4 describes that, the Bragg wavelength $\lambda_B = 1549.9\text{nm} \approx 1550\text{nm}$, the reflectivity value is 0.9999. Now, at the Bragg wavelength, we can compute the value of k_B, which can be represented as,

$$k_B = \frac{\pi \Delta n}{\lambda_B} \quad \text{... (8)}$$

Grating reflectivity strength depends upon the value $k_B L$. Fig. 4 is represented for the $k_B L = 8$, which shows good reflectivity strength, and the value

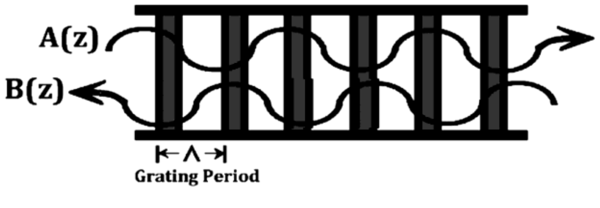

Fig. 3 — Forward and Backward propagation

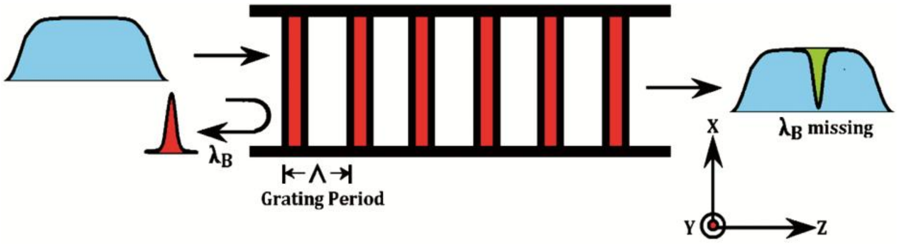

Fig. 2 — Diagram showing fiber Bragg grating

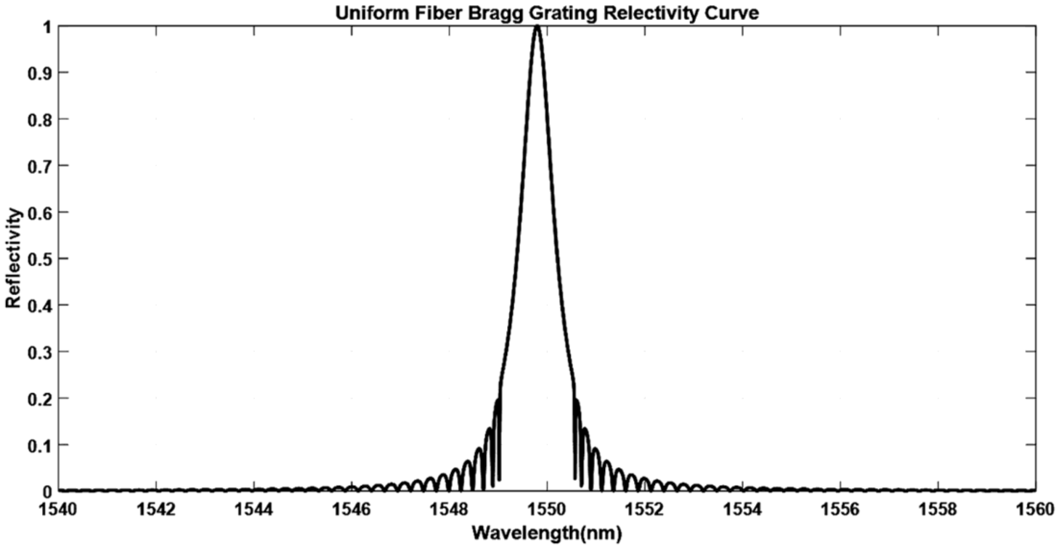

Fig. 4 — Reflectivity Curve of Uniform Fiber Bragg Grating

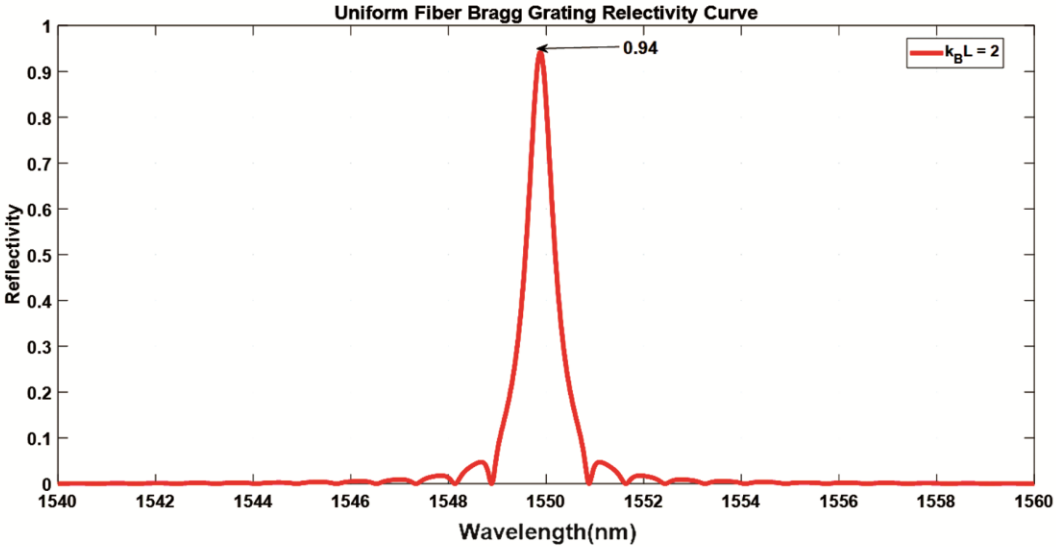

Fig. 5 — Reflectivity of the Uniform Fiber Bragg Grating for the value $K_B L = 2$

of the reflectivity at the Bragg wavelength is 0.9999. Fig. 5 is shown for the $k_B L = 2$. Which shows slightly less reflectivity, of 0.94.

3 The behavior of the optical PSFBG as a switch

In a phase-shifted grating, the cross-phase modulation phenomenon can be utilized to construct all-optical logic gates. The switching effect in the weak continuous wave (CW) is modulated by the pump signal. Analyzing the cross-phase modulation allows observation of the switching effect in the devices. In the proposed approach, various combinations of the pump signal, differing by specific phase shifts, offer different logical functionalities. Both the pump and the controlling optical signal can control the input optical signal of an all-optical switch. The inhomogeneous optical fiber exhibits modulation instability and frequency-chirping phenomena. According to the Kerr effect, the change in the effective index n_{eff} is represented in terms of optical intensity I and non-linear index n_2.

$$n_2 = n + n_2 I \qquad \text{... (9)}$$

The resonance Bragg wavelength undergoes changes due to the Kerr effect. Nonlinear optical fiber Bragg grating switching constitutes a passive switching phenomenon, encompassing XPM switching, self-phase modulation switching, high nonlinear switching, and phase-shifting grating switching. PSFBG offers benefits such as wavelength selectivity, low polarization, and minimal insertion loss. Phase-shifted fibers are typically fabricated using highly nonlinear erbium-doped fiber. The concept of realizing various all-optical logic gates arises when information from the pump signal transforms into a weak continuous-wave light signal. The shift in the input optical power level, induced by the XPM effect, leads to switching between each logic function. Fig. 6 provides a schematic representation of the PSFBG with a high nonlinearity configuration.

Figure 6 illustrates the initial segment of the grating with a length "L" and zero phases. Through the UV laser trimming method, a desired phase shift can be introduced at the center of the grating, resulting in a phase difference of $\Delta\phi$ between the first and second segments. Different logic gates can be designed by employing various phase shifts. The following diagram depicts the fundamental layout design of phase-shifted grating-based all-optical logic gates.

Figure 7 illustrates the layout design of an all-optical logic gate based on PSFBG. In this configuration, a highly amplified pump signal is introduced through port A1 using an erbium-doped fiber amplifier, while the high-power amplified optical signal P_2 enters from port A2. Wavelength division multiplexing (WDM) is employed to couple a CW light into the channel. It is crucial to note that the wavelengths of the pumps are kept away from the photonic band gap, while the weak CW light wavelength is close to it. Consequently, the two pumps will operate in their respective channels, eventually transmitting from the grating's end.

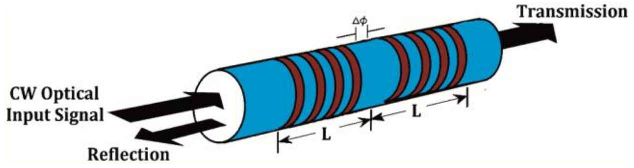

Fig. 6 — Schematic view of the PSFBG

The beat length (L_b) is determined by the equation $L_b = ((\lambda A_{eff}))/((2n_{2B}\,P))$, where L_b reflects the influence of the XPM mechanism. To calculate L_b with a grating length (L) of 2 mm, considering factors such as the wavelength, effective area, refractive index, and power, the value is determined to be 0.7 m as shown in Table 1.

It has been observed that $L_b > L$; thus, it is convenient to disregard the impact of the XPM effects on birefringence. Neglecting the time-related components, Maxwell's electromagnetic theory is employed to derive the coupled equation of the fiber grating as follows:

$$\frac{dA}{dz} = i\delta A + ir_1 B + 2i\gamma\left(\left|X_{p1}\right|^2 + \left|X_{p2}\right|^2\right)A \quad \text{... (10)}$$

$$\frac{dB}{dz} = i\delta B + ir_1 A + 2i\gamma\left(\left|X_{p1}\right|^2 + \left|X_{p2}\right|^2\right)B \quad \text{... (11)}$$

Where A and B, respectively, represent the slow variation amplitude functions of forward and backward propagation in the fiber grating. δ denotes the frequency tuning, and r_1 signifies the coupling coefficient between forward and backward transmitted pulses. X_{p1} and X_{p2} can be expressed as $\sqrt{P_1}e^{i\varphi_1}$ and $\sqrt{P_2}e^{i\varphi_2}$, respectively, where P_1 and P_2 are the light powers of the two pumps, and φ_1 and φ_2 are the initial phases of the two-pump signals. The parameter γ can be defined as $\gamma = ((n_2 * 2\pi))/(\lambda * A_{eff})$, where n_2 is the non-linear coefficient, A_{eff} is the effective area, and λ is the wavelength. Eqs. (10) and (11) can be represented using the matrix method, as shown in Eq. (12).

Table 1 — Parameters to calculate beat length

Wavelength (λ)	1550nm
A_{eff}	10 μm^2
Kerr Co-efficient	$4.5 \times 10^{-16} cm^2/W$
Optical Power	240W

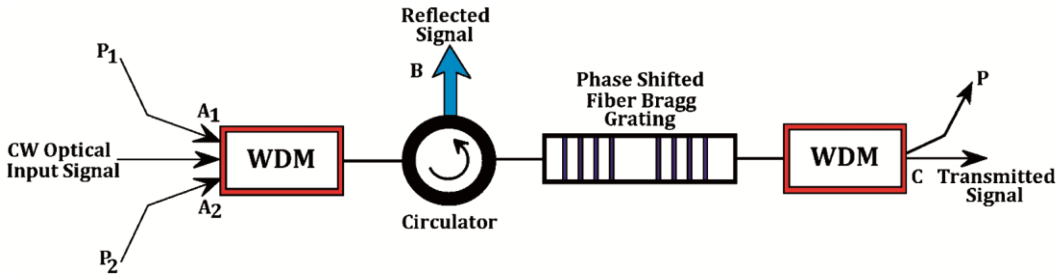

Fig. 7 — Layoutdesignof All-optical logic gate based on PSFBG

$$\frac{d}{dz}\begin{bmatrix}A\\B\end{bmatrix} = iE\begin{bmatrix}A\\B\end{bmatrix} = i\begin{bmatrix}t_1 & r_1\\-r_1 & -t_1\end{bmatrix}\begin{bmatrix}A\\B\end{bmatrix} \quad \text{... (12)}$$

Comparing, $t_1 = 2\gamma(P_1 + P_2) + \delta$, Analyzing the eigenvalues of E, we obtain the eigenvalues.

$$k_1 = k = \sqrt{t_1^2 - r_1^2}, \quad \text{... (13)}$$

$$k_2 = -k = \sqrt{t_1^2 - r_1^2}, \quad \text{... (14)}$$

The first component of the phase-shifted grating's transmission equation may be written as:

$$A_{1L} = A_{10}\left[\cos(kL) + i\left(\frac{t_1}{k}\right)\sin(kL)\right] + iB_{10}\left(\frac{r_1}{k}\right)\sin(kL) \quad \text{... (15)}$$

$$B_{1L} = -iB_{10}\left(\frac{r_1}{k}\right)\sin(kL) + A_{10}\left[\cos(kL) - i\left(\frac{t_1}{k}\right)\sin(kL)\right] \quad \text{... (16)}$$

The following matrix may be utilized to correlate the input and output parts:

$$\begin{bmatrix}A_{1L}\\B_{1L}\end{bmatrix} = \begin{bmatrix}w_{11} & w_{12}\\w_{21} & w_{22}\end{bmatrix}\begin{bmatrix}A_{10}\\B_{10}\end{bmatrix} \quad \text{... (17)}$$

$$\begin{cases} w_{11} = \cos(kL) + i\left(\frac{t_1}{k}\right)\sin(kL)\\ w_{12} = i\left(\frac{r_1}{k}\right)\sin(kL)\\ w_{21} = i\left(\frac{r_1}{k}\right)\sin(kL)\\ w_{22} = \cos(kL) - i\left(\frac{t_1}{k}\right)\sin(kL)\end{cases} \quad \text{... (18)}$$

The FBG's second section contains phase shift as $\phi(z) = \varphi$,

$$\begin{bmatrix}A_{20}\\B_{20}\end{bmatrix} = \begin{bmatrix}e^{i\phi} & 0\\0 & e^{-i\phi}\end{bmatrix}\begin{bmatrix}A_{1L}\\B_{1L}\end{bmatrix} \quad \text{... (19)}$$

Following is a representation of the final matrix:

$$\begin{bmatrix}A_{2L}\\B_{2L}\end{bmatrix} = \begin{bmatrix}e^{i\phi} & 0\\0 & e^{-i\phi}\end{bmatrix}\begin{bmatrix}w_{11} & w_{12}\\w_{21} & w_{22}\end{bmatrix}\begin{bmatrix}w_{11} & w_{12}\\w_{21} & w_{22}\end{bmatrix}\begin{bmatrix}A_{10}\\B_{10}\end{bmatrix}$$

$$\begin{bmatrix}A_{2L}\\B_{2L}\end{bmatrix} = \begin{bmatrix}w_{11}^2e^{i\phi} + w_{12}w_{21}e^{-i\phi} & w_{11}w_{12}e^{i\phi} + w_{12}w_{22}e^{-i\phi}\\ w_{21}w_{11}e^{i\phi} + w_{12}w_{22}e^{i\phi} & w_{22}^2e^{-i\phi} + w_{12}w_{21}e^{i\phi}\end{bmatrix} \quad \text{... (20)}$$

Now, Eq. 20 may be simplified by the following representation:

$$\begin{bmatrix}A_{2L}\\B_{2L}\end{bmatrix} = \begin{bmatrix}W_{11} & W_{12}\\W_{21} & W_{22}\end{bmatrix} \text{ Where, } \begin{cases} W_{11} = w_{11}^2e^{i\phi} + w_{12}w_{21}e^{-i\phi}\\ W_{12} = w_{11}w_{12}e^{i\phi} + w_{12}w_{22}e^{-i\phi}\\ W_{21} = w_{21}w_{11}e^{i\phi} + w_{12}w_{22}e^{i\phi}\\ W_{22} = w_{22}^2e^{-i\phi} + w_{12}w_{21}e^{i\phi}\end{cases} \quad \text{... (21)}$$

After the use of the appropriate boundary condition, B 2L = 0, the results can be obtained as shown below.

$$B_{10} = -\frac{W_{21}}{W_{22}}A_{10}, A_{2L} = \left(W_{11} - \frac{W_{12}W_{21}}{W_{22}}\right)A_{10} \quad \text{... (22)}$$

The transmittance and reflectance parameters that represent switching performance are now defined as follows:

$$T = \left|\frac{A_{2L}}{A_{10}}\right|^2, \text{and } R = \left|\frac{B_{10}}{A_{10}}\right|^2 \quad \text{... (23)}$$

We can calculate the extinction ratio, which is a key variable in determining the system's quality. The extinction ratio is defined as the output power during the on-state divided by the output power during the off-state. The splitting ratio may thus be expressed as follows:

$$E_{AB} = \frac{\int_{-\infty}^{\infty}|A_{2L}|^2}{\int_{-\infty}^{\infty}|B_{10}|^2}, \text{and } E_{BA} = \frac{\int_{-\infty}^{\infty}|B_{10}|^2}{\int_{-\infty}^{\infty}|A_{2L}|^2} \quad \text{... (24)}$$

Based on the extinction ratio, the logic gate's figure of merit may be calculated, and its unit can be expressed as dB,

$$E_{\text{ratio }AB}\ [\text{dB}] = 10\log_{10}E_{AB}, E_{\text{ratio }BA}\ [\text{dB}] = 10\log_{10}E_{BA} \quad \text{... (25)}$$

4 Switching mechanism of PSFBG

Employing a zero-phase shift in the FBG, its switching properties can be analyzed. The high magnitude of the dispersion coefficient poses a challenge to achieving the phase-matching criterion. Consequently, modulation instability can be neglected. The weak CW signal has a wavelength of 1550 nm, while the pump light signals P1 and P2 are assumed to have a wavelength of 850 nm. The detuning of the CW signal is δλ = 0.01 nm, and the non-linear coefficient of the gratings with a phase shift is $\gamma = 1.5 \times (10^3 W^{-1}) / km$. The initial power of the weak CW signal is P_u = 1 mW when measured in this unit. The power of the pump signal varies from 0 to 800 W. The coupling coefficient between the forward and backward propagating signals is denoted as $r_1 = 5\ cm^{-1}$. The proposed unit has an overall length of 4 mm. Fig. 8 illustrates the shift in the transmissivity curve caused by different detunings. Transmissivity and reflectivity are two essential physical characteristics of the device.

Pump power P_1 is introduced from port A_1 along with the low-power CW input signal provided by WDM, while port A_2 receives the pump signal P_2. This results in the overall pump power being $P_1 + P_2$. As the intensity of the pump signal increases, the XPM effect becomes more prominent. The high-quality field being transmitted maintains stability, and the output switches at a value of 229.6 W, as shown in Fig. 9. This 229.6 W power can be considered a threshold pump signal. To achieve the switching effect, the pump power must be higher than this threshold.

The response time (τ_{switch})of optical switches is a further significant factor. We can calculate the parameter τ_{switch} using the full width at half maximum of the system.

$$\tau_{\text{switch}} = \frac{1}{\delta v} = \frac{n_{eff}}{2v\text{I}n_2} \quad \ldots (26)$$

Where "v" stands for the frequency of the incident weak continuous light, Iis known as the consistent input intensity, and n_2 and n_{eff} are the non-linear and effective refractive indices, respectively. In our analysis, we have considered $\text{I} = 7.96 \times (10^{12} W)\ /$

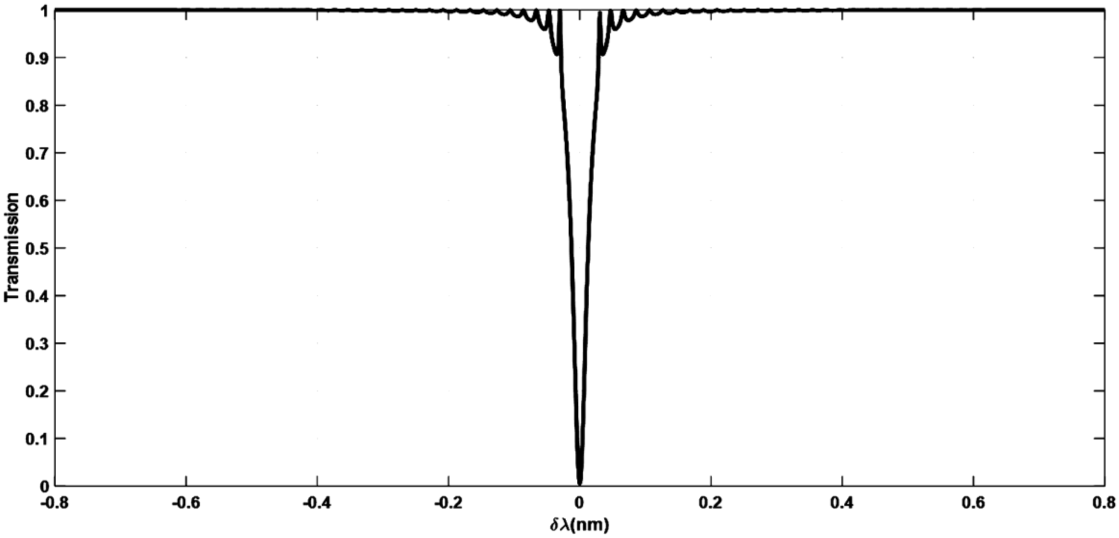

Fig. 8 — Transmission curve of PSFBG as a function of detuning, where $\Delta\phi = 0$

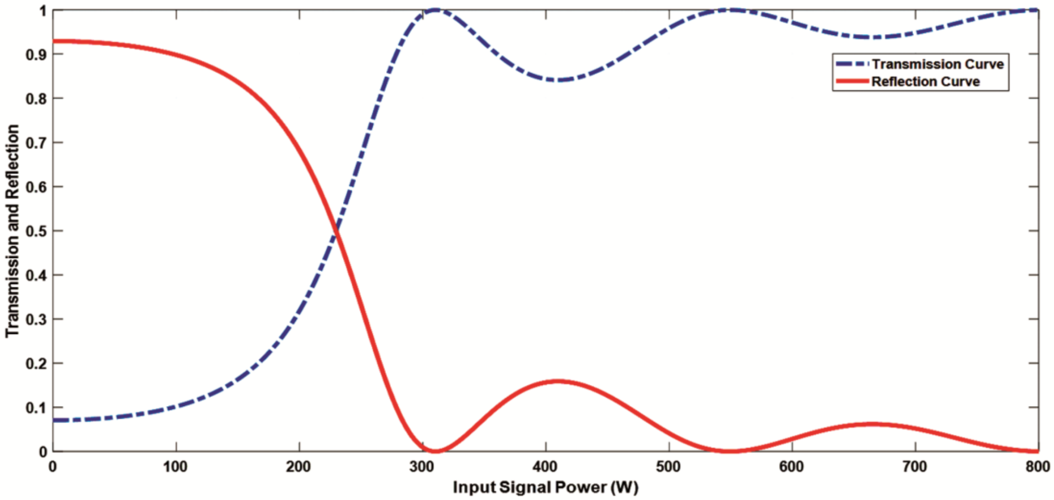

Fig. 9 — Graphical representation of Transmission and Reflection curve as a function of the total pump power

m^2, $n_2 = 5.4 \times (10^{-15} m^2) / W$, $n_{eff} = 1.49$, and $v = 1.93 \times 10^{14} Hz$. The τ_{switch} is approximately 89.8 fs. The transmission and reflection curves in relation to the total pump power are illustrated in Fig. 9.

Figure 10 shows that as the pump power increases, the E_{Ratio} level as a function of the total pump power P when $\Delta\phi = 0$. When the pump power is P = 0, the reflection port B of the Fiber Bragg Gratings with a phase shift receives most of the output power, as depicted in Fig. 7. As the pump power increases beyond the threshold pump power, the E_{Ratio} at reflection port B becomes lower than zero. Conversely, when the pump power decreases below the threshold power, the E_{Ratio} becomes greater than zero. This behavior demonstrates how the signal is shifted from the transmission port to the reflection port by the pump power.

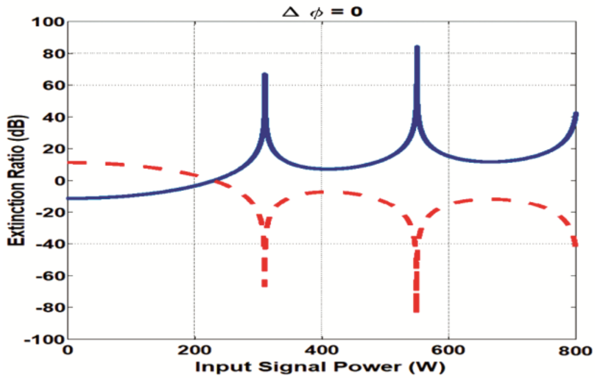

Fig. 10 — Graphical representation of Extinction Ratio(E_{ratio}) level as a function of the total pump power P when $\Delta\phi = 0$

5 Implementation of all-optical Full Adder Circuit using the PSFBG

An all-optical full adder circuit is depicted in Fig. 11, requiring four input signals. Three of these signals are pump signals denoted as P1, P2, and P3, and the fourth signal is a CW optical input signal, where the presence of pump light is represented by "1" with 150 W power, and "0" indicates the absence of pump with 0 W of power. In Fig. 11, WDM is applied to both FBGs with the continuous-wave optical input signal and three control pump signals. To implement the all-optical full adder, two fiber Bragg gratings with different phase shifts are required: FBG1 with a phase shift of π/3 and FBG2 with a zero phase shift. The transmission port C of FBG1 is utilized to retrieve the sum output of the proposed full adder, while the transmission port E of FBG2 is used to obtain the carry output. The total pump power for FBG1 is equal to FBG2, i.e., $P_1 + P_2 + P_3$. Table 2 presents the truth table of the suggested full adder in the all-optical domain.

The transmission and reflection port intensities for the total pump power are presented in Fig. 12 for (a) $\Delta\phi = \pi/3$ for FBG1 and (b) $\Delta\phi = 0$ for FBG2. In Fig. 12(a), the threshold switching occurs at 51.7 W, while Fig. 12(b) indicates that it occurs at 229.6 W. Thus, when the phase shift is increased from $\Delta\phi = 0$ to $\Delta\phi = \pi/3$, a reduction in threshold power is observed. The underlying rationale for this is that switching phenomena require the phase matching requirement, which is essentially the combination of the phase shift of the grating and the phase shift accumulated by the non-linearity. Both must satisfy the phase-matching

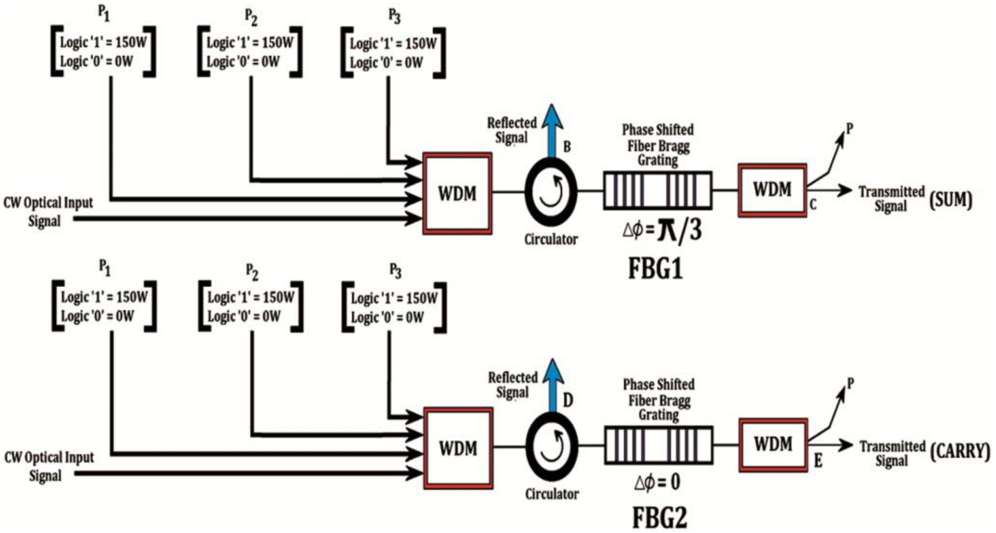

Fig. 11 — Layout of all-optical full adder circuit using the PSFBG Structure

Table 2 — Truth Table of All-Optical Full Adder Circuit using the PSFBG

P_1 (W)	P_2 (W)	P_3 (W)	$E_{ratio\ AB}$ FBG1	$E_{ratio\ BA}$ FBG1	$E_{ratio\ AB}$ FBG2	$E_{ratio\ BA}$ FBG 2	Port C (Transmission Port of FBG1)	Port E (Transmission Port of FBG2)
0 (0W)	0(0W)	0(0W)	-5.17	5.17	-11.19	11.9	0(23.32%)	0(7%)
1(150W)	0(0W)	0(0W)	5.538	-5.538	-7.094	7.094	1(78.16%)	0(16.34%)
0(0W)	1(150W)	0(0W)	5.538	-5.538	-7.094	7.094	1(78.16%)	0(16.34%)
1(150W)	1(150W)	0(0W)	-2.509	2.509	20.11	-20.11	0(35.95%)	1(99.04)
0(0W)	0(0W)	1(150W)	5.538	-5.538	-7.094	7.094	1(78.16%)	0(16.34%)
1(150W)	0(0W)	1(150W)	-2.509	2.509	20.11	-20.11	0(35.95%)	1(99.04)
0(0W)	1(150W)	1(150W)	-2.509	2.509	20.11	-20.11	0(35.95%)	1(99.04)
1(150W)	1(150W)	1(150W)	6.919	-6.191	8.393	-8.393	1(83.11%)	1(83.11%)
							SUM $(P_1 \oplus P_2 \oplus P_3)$	**CARRY** $(P_1P_2 + P2P3 + P1P3$

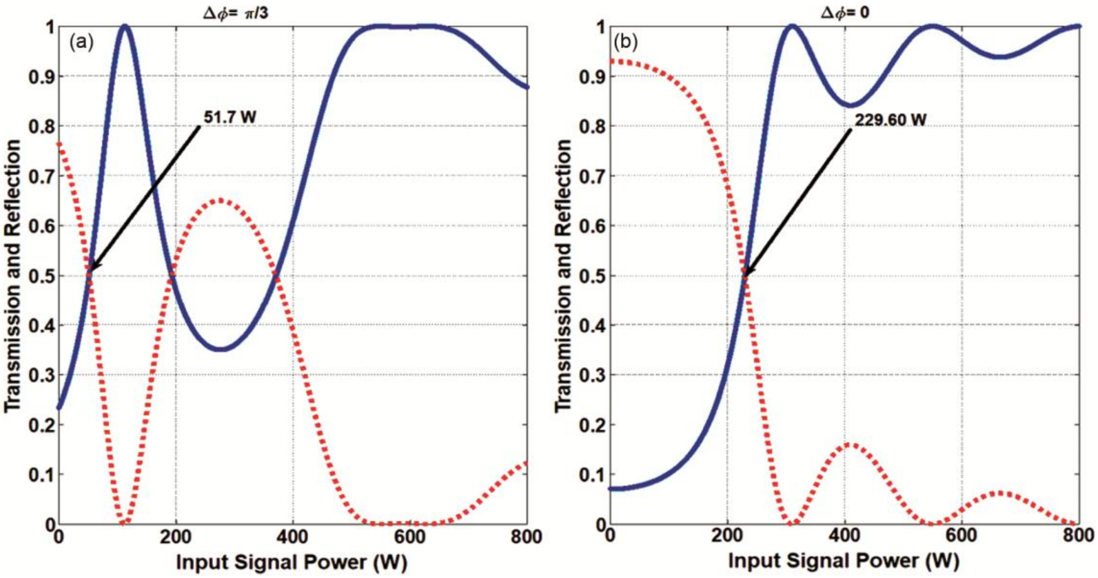

Fig. 12 — Transmission and Reflection curve of the proposed PSFBG for the (a) $\Delta\phi = \pi/3\ for\ FBG1$ (b) $\Delta\phi = 0$ for FBG2

criterion. As the phase shift of the phase-shifted grating increases, the shift in the phase accumulated through non-linearity decreases, leading to a reduced threshold power.

Figure 13 illustrates the ERatio level vs. pump power for (a) $\Delta\phi = \pi / 3$ for FBG1 and (b) $\Delta\phi = 0$ for FBG2. In Fig. 13(a), output switching occurs at 51.7 W, representing the threshold pump power. If the pump power exceeds this threshold, the switching effect is achieved. The ERatio fluctuates with higher pump powers, as observed in Fig. 13(b). Fig. 13(a) further shows that FBG with a phase shift directs maximum output power toward reflection port B when the pump power is zero. However, the power decreases at reflection port B to less than 0 if the pump signal power exceeds the threshold, causing Eratio to be greater than zero. This indicates that when pump power is applied, the signal switches from the reflection port to the transmission port. From Fig. 13(b), it is evident that when the pump power P exceeds 229.6 W, $Eratio_{AB}$ is greater than zero. If the pump power is less than 229.6 W, $Eratio_{AB}$ is less than zero. Considering the threshold powers for both FBG1 and FBG2 as 51.7 W and 229.6 W, respectively, input control power values P1, P2, and P3 are chosen to enable FBG1 to function as an EXOR gate, FBG2 as an AND gate, and the combined unit as a full adder. Thus, P1, P2, and P3, with logic 1 as 150 W and logic 0 as 0 W, realize the PSFBG-based all-optical full adder (EXOR and AND gates). Table 2 serves as the truth table for PSFBG, with $\Delta\phi = \pi / 3$ (FBG1) functioning as an EXOR gate at port C and $\Delta\phi = 0$ (FBG2) functioning as an AND gate at port E.

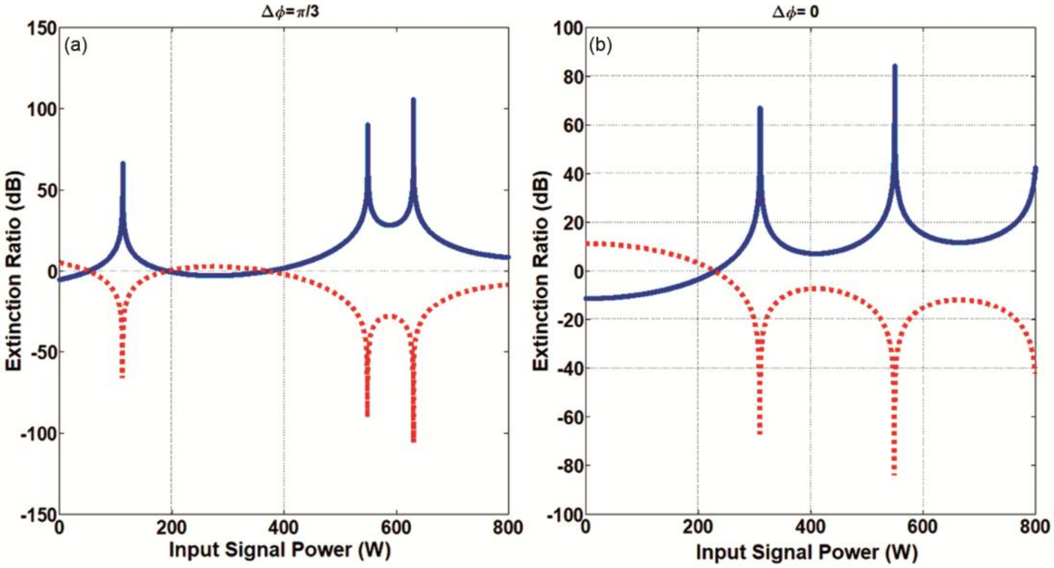

Fig. 13 — Variation of E_{Ratio} level as a function of the total pump power P with the for the (a) $\Delta\phi = \pi/3$ for FBG1 (b) $\Delta\phi = 0$ for FBG2

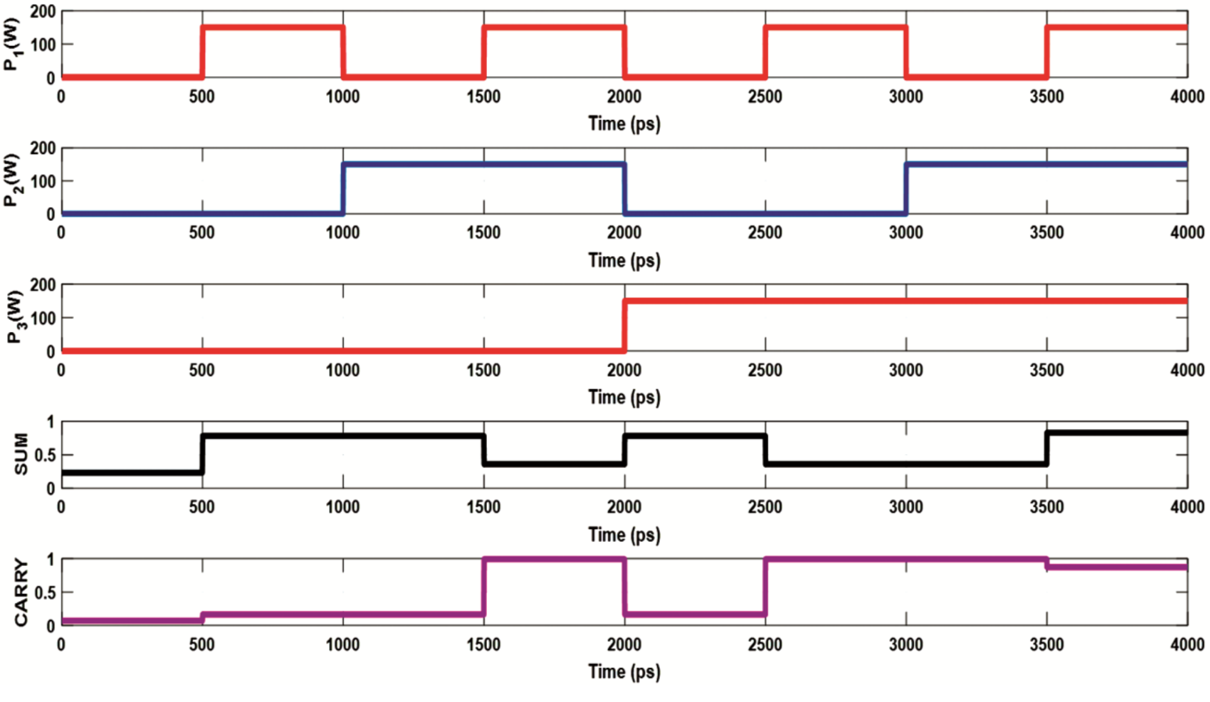

Fig. 14 — Time domain response of all-optical Full Adder using the PSFBG

Figure 14 depicts the time-based simulation of an all-optical full adder. Rows one to three show input power changes ($P_1, P_2,$ andP_3), the fourth row displays the SUM output, and the fifth row shows the CARRY output. All combinations from Table 2 demonstrate the effective functioning of the FBG-based design in Fig. 11 as an all-optical full adder. For input (000), where $P_1, P_2,$ andP_3 are 0 W, FBG1 significantly reflects CW light ($E_{ratioAB}$: −5.7 dB, reflectivity: 78.85%). Valid (logical value 1) if transmissivity or reflectivity is above 70%; invalid (logical value 0) if below 40%, resulting in port C (SUM) OFF (0) and port B ON (1). FBG2 reflects ($E_{ratioAB}$: −11.19 dB, reflectivity: 93.95%), resulting in port E (CARRY) OFF (0) and port D ON (1). For input (010) – P_1 at 0 W, P_2 at 150 W, and P_3 at 0 W - FBG1 transmits

($E_{ratioAB}$: 5.538 dB, transmissivity: 78.16%). Port C (SUM) is ON (1), port B is OFF (0). FBG2 reflects ($E_{ratioAB}$: -7.094 dB, transmissivity: 16.34%), resulting in port E (CARRY) OFF (0) and port D ON (1).For input (110) – P_1, P_2 at 150 W, P_3 at 0 W - FBG1 reflects ($E_{ratioAB}$: -2.509 dB, transmissivity: 35.95%). Port C (SUM) is OFF (0), port B is ON (1). FBG2 transmits ($E_{ratioAB}$: 20.11 dB, transmissivity: 99.04%), resulting in port E (CARRY) ON (1) and port D OFF (0).

For input (001) - P_1, P_2 at 0 W, and P_3 at 150 W - FBG1 transmits ($E_{ratioAB}$: 5.538 dB, transmissivity: 78.16%). Port C (SUM) is ON (1), port B is OFF (0). FBG2 reflects ($E_{ratioAB}$: -7.094 dB, transmissivity: 16.34%), resulting in port E (CARRY) OFF (0) and port D ON (1).

For input (100) – P_1 at 150 W, P_2, P3 at 0 W - FBG1 transmits ($E_{ratioAB}$: 5.538 dB, transmissivity: 78.16%). Port C (SUM) is ON (1), port B is OFF (0). FBG2 reflects ($E_{ratioAB}$: -7.094 dB, transmissivity: 16.34%), resulting in port E (CARRY) OFF (0) and port D ON (1). For input (101) – P_1 at 150 W, P_2 at 0 W, and P_3 at 150 W - FBG1 reflects ($E_{ratioAB}$: -2.509 dB, transmissivity: 35.95%). Port C (SUM) is OFF (0), port B is ON (1). FBG2 transmits ($E_{ratioAB}$: 20.11 dB, transmissivity: 99.04%), resulting in port E (CARRY) ON (1) and port D OFF (0).For input (011) – P_1 at 0 W, P_2, P_3 at 150 W - FBG1 reflects ($E_{ratioAB}$: -2.509 dB, transmissivity: 35.95%). Port C (SUM) is OFF (0), port B is ON (1). FBG2 transmits ($E_{ratioAB}$: 20.11 dB, transmissivity: 99.04%), resulting in port E (CARRY) ON (1) and port D OFF (0).For input (111) –P_1, P_2, P_3 at 150 W - FBG1 transmits ($E_{ratioAB}$: 6.919 dB, transmissivity: 83.11%). Port C (SUM) is ON (1), port B is OFF (0). FBG2 transmits ($E_{ratioAB}$: 8.393 dB, transmissivity: 83.11%), resulting in port E (CARRY) ON (1) and port D OFF (0).

6 Implementation of an all-optical Full Subtractor circuit using the PSFBG

Figure 15 illustrates the proposed configuration for an all-optical full subtractor, utilizing four input signals. The fourth signal corresponds to the continuous wave (CW) optical input, represented by "1" when the 150 W pump light is present and "0" when absent. Crucial components in this configuration are six phase-shifted fiber Bragg gratings (PSFBGs): FBG1 (π/3 phase shift), FBG2 (3π/2 phase shift), FBG3, FBG4, FBG5 (zero phase shift), and FBG6 (3π/2 phase shift). The functionality of the subtractor is outlined in Table 3. The FBG-based subtractor comprises FBG1 to FBG6, and the pump powers $P_1, P_2,$ andP_3, along with the CW optical input signal, act as inputs to the WDM of FBG1. Fig. 15 details the derivation of one subtractor output (difference) from the transmission port B of

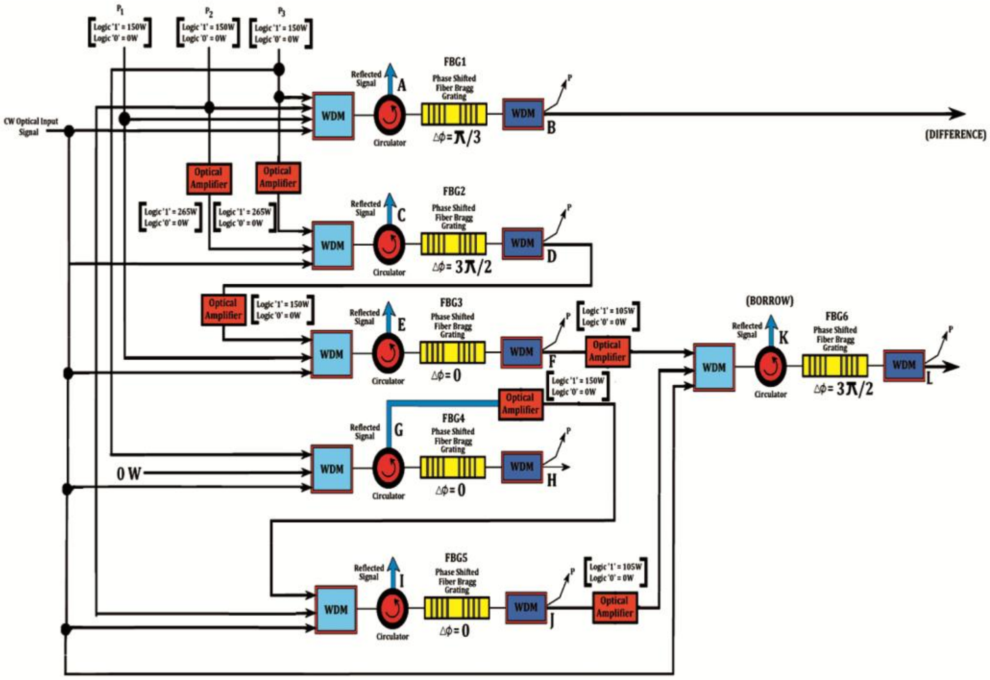

Fig. 15 — Layout Design of All-optical Full-Subtractor circuit using three PSFBG structures

Table 3 — Truth Table of All-Optical Full Subtractor Circuit using the PSFBG

P_3 (W)	P_2 (W)	P_1 (W)	Port B (Transmission Port of FBG1) (Difference)	Port K (Reflection Port of FBG6) (Borrow)
0(0W)	0(0W)	0 (0W)	0 (23%)	0 (27.84%)
0(0W)	0(0W)	1(150W)	1 (74.04%)	1 (76.42%)
0(0W)	1(150W)	0(0W)	1 (74.04%)	1 (72.49%)
0(0W)	1(150W)	1(150W)	0 (36.7%)	1 (76.93%)
1(150W)	0(0W)	0(0W)	1 (74.04%)	0 (6.67%)
1(150W)	0(0W)	1(150W)	0 (36.7%)	0 (29.05%)
1(150W)	1(150W)	0(0W)	0 (36.7%)	0 (37.71%)
1(150W)	1(150W)	1(150W)	1 (88.8%)	1 (77.84%)

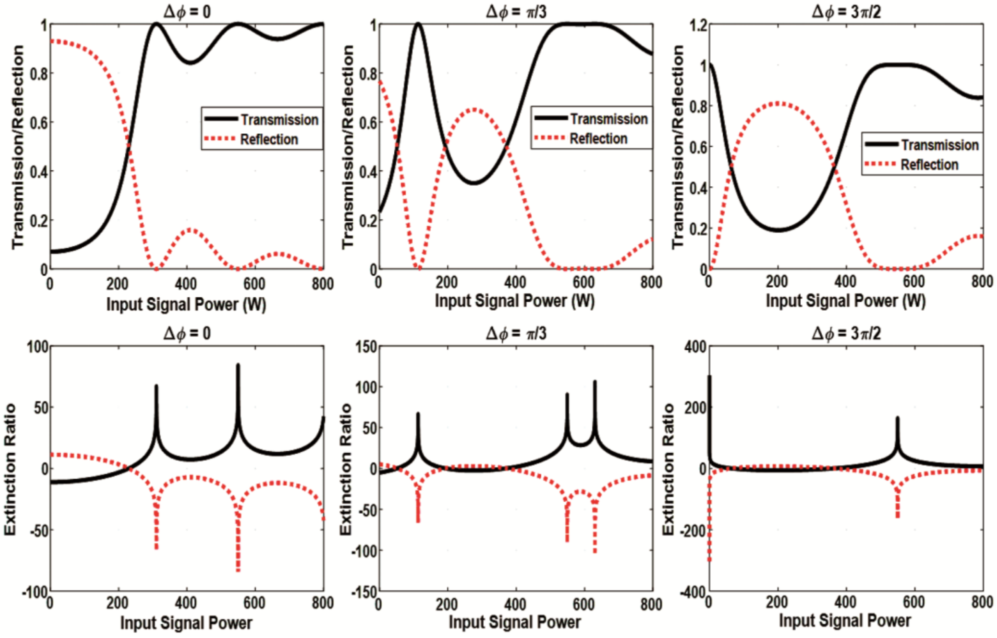

Fig. 16 — Variation of Reflectivity/ Transmissivity and E_{Ratio} level as a function of the total pump power P for the $\Delta\phi = 0, \Delta\phi = \pi/3$ and $\Delta\phi = 3\pi/2$

FBG1. The WDM of FBG2 receives inputs from pump powers P_2 and P_3, resulting in an amplified pump power of 256 W. Additionally, the CW optical input signal is applied to the WDM of all FBGs. The transmission port D of FBG2 feeds into the WDM of FBG3 (with $\Delta\phi = 0$), while the WDM of FBG4 takes inputs from P_3, 0 W pump power, and the CW optical signal, with a phase shift of $\Delta\phi = 0$.WDM inputs of FBG5 include the reflection port G output (connected to an optical amplifier), P_2, and the CW optical signal, all with $\Delta\phi = 0$. The transmission port J output, amplified to 105 W, serves as one input to the WDM of FBG6, along with the CW optical input signal. The WDM of FBG6 also receives inputs from the amplified output of transmission port F. The reflection port K of FBG6 produces the borrow output of the full subtractor.

Figure 16, the variation of Eratio levels with the total pump power P is demonstrated for different phase shifts ($\Delta\Phi = 0$ for FBG3, FBG4, and FBG5; $\Delta\Phi = \pi/3$ for FBG1; $\Delta\Phi = 3\pi/2$ for FBG2 and FBG6). It provides insights into the threshold switching power requirements for FBG1 (51.7 W) and FBG2 (63.1W), enabling precise pump power selection. Utilizing 150 W as logic 1 and 0 W as logic 0, the optical signal eqivalent to EXOR logic is generated at the transmission port of FBG1, and the reflection port of FBG6.

For the input (000), where P_3, P_2, and P_1 are 0 W, most CW light is reflected at port A, yielding valid logic 1 for transmissivity above 70%. This results in port B (DIFFERENCE) OFF (0) and port A ON (1). For the input (001), with P_3, P_2 at 0 W, and P_1 at 150 W, port B transmits the majority of CW light.

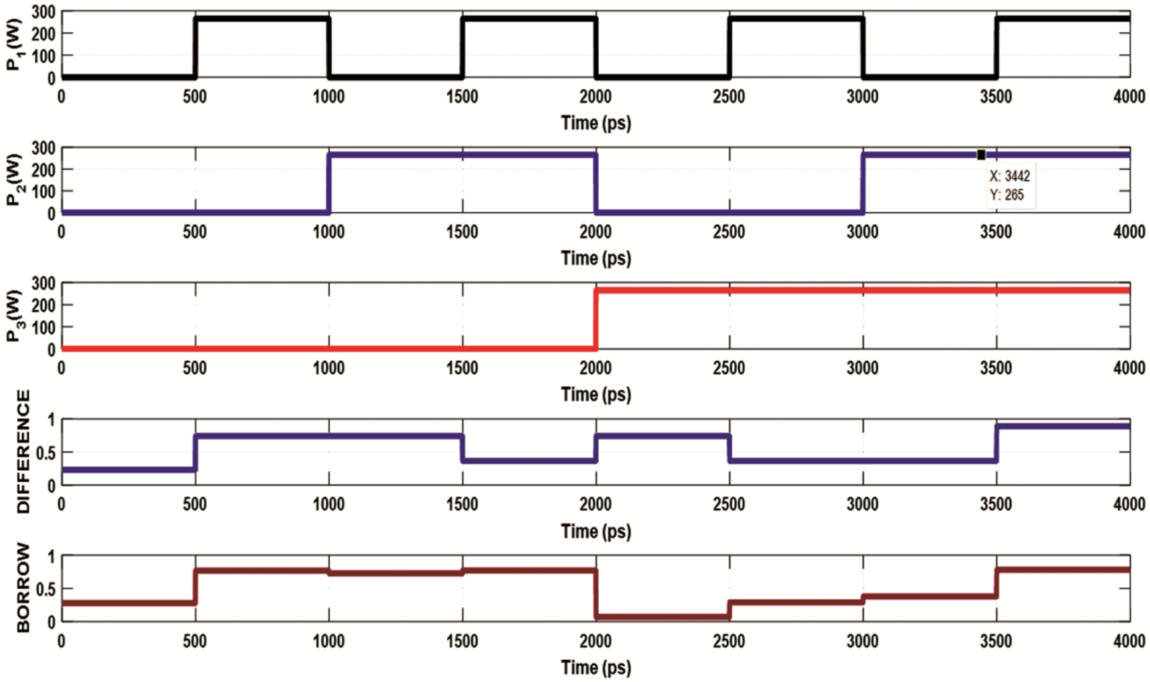

Fig. 17 — Time domain response of all-optical Full Subtractor circuit using the PSFBG

Transmissivity at 74.04% marks port B ON (1), while port A is OFF (0). For the input (010), with P_3 at 0 W, P_2 at 150 W, and P_1 at 0 W, port B communicates most CW light, leading to port B ON (1) and port A OFF (0). For the input (011), with P_3 at 0 W, P_2 at 150 W, and P_1 at 150 W, port B reflects the majority of CW light, resulting in port B OFF (0) and port A ON (1).

For the input (100), with P_3 at 150 W, P_2, and P_1 at 0 W, port B communicates most CW light, making port B ON (1) and port A OFF (0). For the input (101), with P_3 at 150 W, P_2 at 0 W, and P_1 at 150 W, port B reflects the majority of CW light, leading to port B OFF (0) and port A ON (1). For the input (110), with P_3, P_2 at 150 W, and P_1 at 0 W, port B reflects most CW light, resulting in port B OFF (0) and port A ON (1). For the input (111), with $P_3, P_2,$ and P_1 at 150 W, port B communicates most CW light, making port B ON (1) and port A OFF (0).

The time-domain response of an all-optical full subtractor using PSFBG as shown in Fig. 17.

7 Conclusion

We have proposed a design for an all-optical full adder and subtractor using a PSFBG, which is constructed using erbium-doped fiber. A detailed discussion on the coupled mode theory of fiber Bragg gratings for determining transmission and reflection characteristics has been presented. Additionally, we observed that various pump lights can control the switching of a CW light. Consequently, information from the pump light is transmitted to the CW light by managing different combinations of pump lights. In the simulation, the presence of the pump light at the input port is represented by "1," while the absence of the pump light is denoted by "0." By altering the combination of various pumps, we have successfully implemented an all-optical full adder in a fiber grating with π/3 and zero phase shift. Furthermore, using PSFBG with π/3, 2π/3, and zero phase shifts, the full subtractor circuit can be realized. The theoretical study of the all-optical full adder and subtractor, based on XPM in a PSFBG, is presented in this paper. The threshold power of switching can be reduced by altering the phase shift of fiber gratings. The proposed designs hold promise for future applications in communication systems and optical integrated circuits.

References

1 Silberberg Y, Perlmutter P & Baran J E, *Appl Phys Lett*, 51 (1987) 1230.
2 Papadimitriou G I, Chrisoula P & Andreas S P, *J Lightwave Technol*, 21 (2003) 384.
3 Chai Z, *et al*., *Adv Opt Mater*, 5 (2017) 1600665.
4 Sasikala V & Chitra K, *J Opt*, 47 (2018) 307.
5 Nozaki K, *et al*., *Nature Photon*, 4 (2010) 477.
6 Volz T, *et al*., *Nature Photon*, 6 (2012) 605.

7 Mizrahi V, *et al.*, *Opt Lett,* 14 (1989) 1140.
8 Singh G, Yadav R P & Janyani V, *New Adv Technol*, (2010).
9 Kumar S, Raghuwanshi S K & Kumar A, *Opt Eng,* 52 (2013) 097106.
10 Zhang M, *et al.*, *Appl opt,* 55 (2016) 4418.
11 Kumar A, Kumar S & Raghuwanshi S K, *Optik,* 125 (2014) 5764.
12 Kumar S, *et al.*, *Appl Opt,* 54 (2015) 8479.
13 Kumar A, Kumar S & Raghuwanshi S K, *Opt Commun,* 324 (2014) 93.
14 Yadav A, Kumar A & Prakash A, *Mater Today: Proc,* 56 (2022) 462.
15 Kaur S, Singh M L & Singh M, *Opt Quant Electron,* 54 (2022) 341.
16 Pal A, Kumar S & Sharma S, *Photon Net Commun,* 35 (2018) 79.
17 Hill M T, *et al*., *Microwave Opt Technol Lett,* 31 (2001) 411.
18 Kumar S, *et al*., *Appl Opt,* 54 (2015) 6397.
19 Kumar S, Raghuwanshi S K & Rahman B M A, *Opt Quant Electron,* 47 (2015) 3509.
20 Raghuwanshi S K, Kumar A & Chen N K, *Opt Commun,* 333 (2014) 193.
21 Ding M, *et al.*, *IEEE J Select Top Quant Electron,* 24 (2017) 1.
22 Roy J N, *Optik*, 120 (2009) 318.
23 Kim J Y, *et al*., *J Lightwave Technol,* 24 (2006) 3392.
24 Singh P, *et al*., *Opt Quant Electron,* 48 (2016) 1.
25 Kaur S, *Optik-Int J Light Electron Opt,* 124 (2013) 2650.
26 Nair N, Kaur S & Singh H, *Optik*, 231 (2021) 166325.
27 Li H, *et al*., *Opt Lasers Eng,* 112 (2019) 1.
28 Sun H, *et al*., *Opt Fiber Technol*, 18 (2012) 425.
29 Rakshit J K, Chattopadhyay T & Roy J N, *Optik,* 124 (2013) 6048.
30 Kumar A, *Opt Quant Electron*, 48 (2016) 1.
31 Li L & Junqiang S, *J Mod Opt,* 59 (2012) 1149.
32 Rakshit J K, Chattopadhyay T & Roy J N, *J Theoret Appl Phys,* 1 (2013) 32.
33 Gayen D K, Pal R K & Roy J N, *Chin Opt Lett,* 7 (2009) 530.
34 Kumar A & Raghuwanshi S K, *Optik*, 127 (2016) 8751.
35 Chen Q, *et al*., *Opt Lett*, 39 (2014) 4255.
36 Bharti G K & Rakshit J K, *Photon Net Commun*, 35 (2018) 381.
37 Bharti G K & Sonkar R K, *Opt Quant Electron,* 54 (2022) 176.
38 Kumar A, *et al*., *Appl Phys B*, 127 (2021) 1.
39 Mahanty S & Kumar A, *Brazil J Phys,* 52 (2022) 69.
40 Kwon M S & Steier W H, *Opt Exp,* 16 (2008) 9372.
41 Biswas U, Jayanta K R & Bharti G K, *Opt Quant Electron,* 52 (2020) 1.
42 Yadav A, Kumar A & Prakash A, *Optik*, 288 (2023) 171190.
43 Agrawal G P, Fiber Gratings, in Applications of Nonlinear Fiber Optics, *Elsevier*, (2008) 1.
44 Li Q, Song J, *et al.*, *Appl Opt*, 55 (2016) 6880.